PHYSICAL REVIEW B **106**, 184303 (2022)

Anomalous thermal response of bulk diamond to uniaxial (100) strain: A first-principles prediction

Biao Wang,[1] Jiwen Zhao,[1] Yanwei Hu,[2] Yurong He,[2] Nikolay Rodionov,[3] Jiecai Han,[1] and Jiaqi Zhu[1,4,*]

[1] *National Key Laboratory of Science and Technology on Advanced Composites in Special Environments, Harbin Institute of Technology, Harbin 150080, China*
[2] *School of Energy Science & Engineering, Harbin Institute of Technology, Harbin 150001, China*
[3] *State Research Center of Russian Federation, Troitsk Institute for Innovative and Fusion Research, Troitsk, Moscow 108840, Russia*
[4] *Key Laboratory of Micro-systems and Micro-structures Manufacturing, Ministry of Education, Harbin 150080, China*

(Received 2 September 2022; revised 1 November 2022; accepted 8 November 2022; published 18 November 2022)

Diamond, a material that exhibits ultrahigh thermal conductivity with a sensitive thermal response to stress, is an ideal heat-sink material in the embedded cooling paradigm. This study uses first-principles calculations with the phonon Boltzmann transport equation to predict the variation rules of the thermal conductivity of diamond along the ⟨100⟩ crystal direction under strains at three orders of magnitude: 0.1%, 1%, and 10.5%. Density functional theory is used to predict the stress–strain dependence of diamond and the temperature-dependent thermal conductivity of unstrained diamond. The predictions are in good agreement with the experimental results. The calculated uniaxial strain–thermal conductivity dependence results reveal that the thermal conductivity of diamond abnormally increases by approximately 15% under small-scale uniaxial strain because of the weakened anharmonic interatomic force constants. Under large-scale strain, the thermal conductivity considerably decreases because of reduced phonon group velocities and increased numbers of phonon scattering channels. The findings in this study will guide analyses of the dependence of thermal conductivity on strain in other diamondlike structures, such as Group IV element-based materials. The abnormal thermal response at small strain is expected to lead to the realization of an artificial thermal conduction channel.

DOI: 10.1103/PhysRevB.106.184303

I. INTRODUCTION

Diamond, a crystalline material composed of carbon, has an extraordinarily high thermal conductivity (κ), which benefits from high acoustic velocities and weak phonon–phonon Umklapp (U) scattering based on its strong sp^3 bond stiffness between carbon atoms and light atomic mass [1]. The power density requirement of the electronic components is increasing with their rapidly increasing integration, miniaturization, and performance. Diamond has become an ideal heat-sink material in the embedded cooling paradigm, which is a third-generation thermal management technology [2]. Currently, microwave plasma-assisted chemical vapor deposition [3] and high-temperature and high-pressure methods [4] are used to synthesize diamond in large quantities. Ralchenko *et al.* prepared high-purity synthetic single-crystalline diamonds (of natural carbon isotope composition) that exhibited the highest κ-value of 2400 W m^{-1} K^{-1} at room temperature [5]. Diamond is the ceiling in terms of the thermal conductivity of natural materials. However, there are efforts to regulate or exceed this thermal conductivity limit. Strain is an effective tool for adjustment of the physical properties of diamond [6,7,8]. Anomalous physical properties in diamond can be obtained by changing the crystal lattice and the distribution of electrons around the carbon nucleus through the application of stress. Dang *et al.* [6] achieved sample-wide uniform elastic strains in a microfabricated diamond under uniaxial tensile loading at room temperature. Liu *et al.* [7] predicted the emergence of superconductivity in a compression shear-strained diamond crystal. Additionally, Broido *et al.* [8] found that diamond thermal conductivity was improved nearly fivefold at the high compressive hydrostatic pressure of 400 GPa. Thus, there is considerable value in further exploration of the effect of strain engineering on diamond thermal conductivity.

Three-dimensional bulk materials and two-dimensional (2D) materials under isotropic tensile stress or compressive hydrostatic pressure have been extensively studied. Although the rules are different, strain can significantly alter κ and its behavior by changing phonon lifetimes, group velocities, heat capacities, and dispersion relationships [9]. For bulk materials, the enhancement of isotropic pressure or reduction of tension generally causes the lattice constant to decrease, group velocities to increase, intrinsic phonon scattering to decrease, and κ to increase [8,10,11,12]. Tang and Dong [10] calculated the κ of MgO in the pressure and temperature ranges of 0–150 GPa and 300–4000 K; their values match the values of the mantle. The same rule was found in an experimental study by Dalton *et al.* [11]. First-principles calculations by Broido *et al.* [8] revealed that diamond thermal conductivity had a positive pressure dependence. In that study, hydrostatic pressure improved the frequencies of longitudinal acoustic (LA) and optical phonon modes, thereby decreasing their populations. The increase in κ under hydrostatic pressure

---

[*] zhujq@hit.edu.cn

was primarily because of the decrease in the phonon–phonon scattering rate. Parrish [12] predicted the strain-dependent phonon properties of a soft system and found that the κ of Lennard-Jones argon decreased monotonically from compression to tension because of decreased phonon lifetimes and group velocities. Although the dependence of boron arsenide κ on pressure has a similar trend, it is very weak because of the weak pressure dependence of phonon–phonon scattering rates [13]. However, the relationship between κ and strain is not always monotonous in all bulk materials because of synergy among many factors. For example, silicon exhibits anomalous behavior; the silicon κ is constant when compressed (0–0.03) and begins to decline only when the system is stretched [12]. During decompression, the effects of increased phonon lifetimes and group velocities on κ neutralize the effect of reduced heat capacity on κ; thus, κ is generally stable. When silicon is under tensile stress, the heat capacity dominates and κ decreases. Additionally, the authors of a review [9] noted that κ decreased with increasing pressure in large mass difference compounds because of increased intrinsic phonon scattering rates [14]; it decreased in HgTe and CuCl [15,16] because of pressure-induced phase transitions.

In 2D materials, pressure can cause corrugation of the 2D layer [17]; thus, it is more useful to study the effect of tensile stress on κ. 2D materials include silicene, graphene, MoS_2, and the recently developed diamane [18]. The κ and strain dependence of 2D materials are often complex and abnormal. The κ of small graphene [19] minimally varies with tensile strain and slightly decreases because of the synergistic effect of altered harmonic interatomic force constants (IFCs) and weakened anharmonic IFCs. As the system size increases, κ generally diverges for both silene and graphene [20,21]. For large samples, κ initially increases with tensile strain, which is largely related to the hardening of out-of-plane acoustic modes (ZA modes) [20,22]. The subsequent competition between the reduced heat capacity of the mode and the increased lifetime of a ZA phonon results in a κ peak [23]. Kuang *et al.* [21] found that long-wavelength ZA phonons had a dominant role in the thermal transport of strained graphene, which is responsible for κ divergence and a strong size effect. This divergence is mutative and related to the abrupt dispersion transition in the long-wavelength limit, which can be analytically determined using the elastic theory of a thin plate [20,24]. In contrast to silicene and graphene, the κ of MoS_2 decreases monotonically under tensile strain, which leads to phonon vibration softening [17,25] and a red shift in the major peak of the vibrational density of state. Moreover, Ding *et al.* [25] found that κ was not influenced by any obvious coupling between defects and strains of MoS_2. Additionally, a substantial effect of strain on the hydrodynamic behavior of phonons was found in diamane [26]. For some common 1D materials, such as silicon nanowires and diamond nanowires, the variation of κ with strain is generally similar to the variation in corresponding bulk materials [12].

The findings in the present study indicate that the isotropic strain process has distinct effects on the κ values of various materials; there are unusual phenomena at special state points. Additionally, different tensile scales typically affect κ and its underlying mechanisms. There appears to be a consensus among researchers that isotropic mechanical tension has a negative effect on the thermal transport of 3D materials in terms of softening phonon modes, reducing phonon group velocities, and reducing phonon lifetime, particularly for diamonds.

Although it is difficult to implement isotropic strain in practice, the application of uniaxial strain is easier. Uniaxial stretching usually results in anisotropic physical responses, compared with isotropic stretching. Furthermore, the variation rule of physical properties caused by uniaxial stretching sometimes differs from the variation rule caused by isotropic stretching. Hu *et al.* [27] found an anomalous thermal response of silicene after uniaxial stretching; under tensile strain, its κ significantly increased, then fluctuated at an elevated plateau. These findings result from the interaction between two competing mechanisms of silicene heat conduction. Pereira *et al.* [28] confirmed that the divergence predicted for isotropically strained graphene also occurred under uniaxial strain at finite temperature; it was confined to the strain direction. With respect to bulk materials, Seijas-Bellido *et al.* [29] compared the responses of ZnO κ under isotropic and uniaxial pressures. Under hydrostatic strain, the change in κ mainly resulted from the change in phonon relaxation time. For uniaxial compressive strain, the contribution of phonon relaxation time was balanced by increased group velocities; thus, κ was less affected by strain. The diamond κ under uniaxial deformation has not been studied thus far. There is a need to determine whether variations in diamond κ under uniaxial strain follow the same rule as its variations under isotropic strain. There is also a need to determine the anisotropy variation rule of diamond κ under uniaxial strain. Diamond κ is very important for efficient heat dissipation and thermal management of diamond-based electronic devices. Therefore, analyses of diamond κ have important theoretical and practical implications. The findings provide important insights for diamond growth with controllable stress on devices to be cooled.

In this paper, the diamond κ under uniaxial strain is predicted using a first-principles approach combined with an exact solution of the linearized phonon Boltzmann transport equation (BTE). The method achieves sufficiently high material fidelity without the need for empirical and semiempirical potentials, compared with the nonequilibrium molecular-dynamics method and the equilibrium Green-Kubo approach [30]. The stress–strain and strain–thermal conductivity relationships in diamond are obtained in this study. There is an abnormal thermal response under small-scale (SS) strain. Through analyses of phonon behavior, we clarify the thermal response mechanisms of diamond under different scale strains. Our results will guide studies of the dependence of thermal conductivity on stress in other diamondlike structures, such as Group IV element-based materials.

II. COMPUTATIONAL METHODS

Density functional theory (DFT) is used to optimize the lattice structure (fixation in the z direction and relaxation in the x and y directions) and calculate IFCs. The linearized BTE is used to predict the thermal conductivity of diamond under stress.

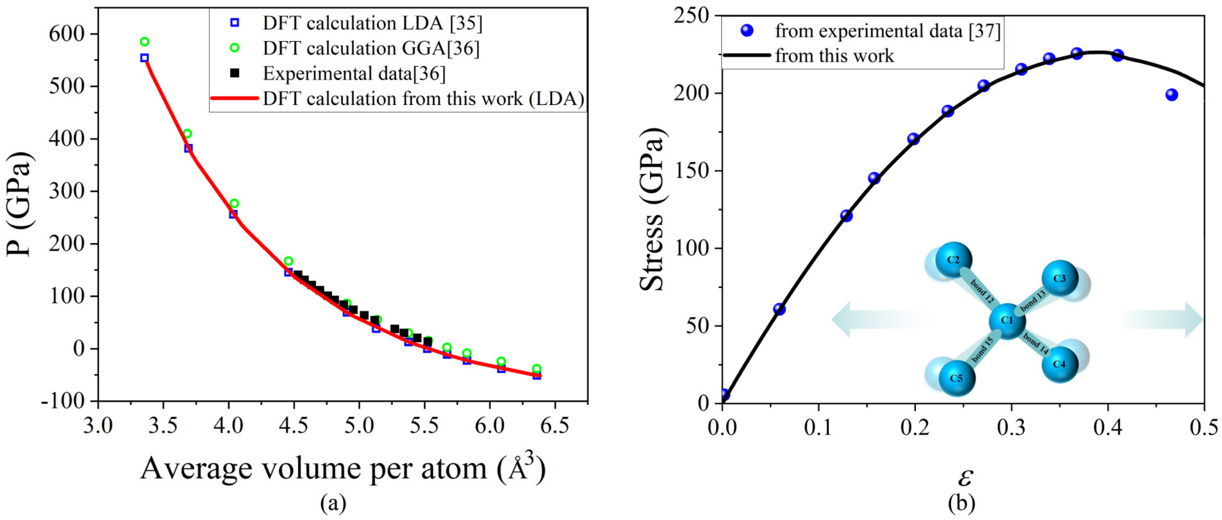

(a) (b)

FIG. 1. Stress-strain relationships in diamond. (a) Isotropic strain and (b) uniaxial strain along the ⟨100⟩ crystal direction.

All first-principles calculations, carried out using the *Vienna ab initio Simulation Package* with the projector augmented wave method [31,32] and the local density approximation (LDA) [33], are used to describe exchange-correlation effects. The plane wave cutoff energy is set to 520 eV. The force is regarded as the convergence criterion, and the structural optimization is stopped when the force of all atoms is $< 10^{-6}$ eV Å^{-1}. The first Brillouin zone is sampled with $16 \times 16 \times 16$ Monkhorst-Pack [34] k-point grids. In the process of structural optimization, the diamond unit cells are allowed to relax only in the x and y directions. Mechanical properties are examined by conducting uniaxial tensile and hydrostatic pressure loading simulations. The stress–strain relationships in diamond under stress are shown in Fig. 1. In Fig. 1(a), the DFT calculation from this work (red solid line) is in good agreement with the DFT calculation with LDA (blue hollow squares) from Kunc *et al.* [35]. However, it is approximately 1% less than the lattice constant measured for diamond [36] because the LDA has a tendency to overbind [8]. In contrast, the generalized gradient approximation has a tendency to overestimate. There may be slight differences in results with either the LDA or the generalized gradient approximation, but the main findings in this paper are not affected. The stress–strain relationships for uniaxial stress along the ⟨100⟩ crystal direction are shown in Fig. 1(b); the DFT results are in good agreement with the experimental data [37]. Previous studies concerning strain–thermal conductivity dependence usually used strain between 1.0% and 10.0% [12,17,20,22,25]. The subsequent calculation mainly analyzes the effects of three uniaxial stress conditions (i.e., 1.076, 10.881, and 101.411 Gpa) on the thermal conductivity of diamond. Their corresponding strains span three orders of magnitude: 0.1%, 1.0%, and 10.5%, respectively.

Table I presents the calculated bond lengths and bond angles for the different scale strains. In this paper, we use $\varepsilon = \frac{l - l_0}{l_0}$ to denote the dependent variable. Positive numbers indicate stretching and negative numbers indicate compression; l_0 and l represent sample length in the strain direction before and after strain application, respectively.

Density functional perturbation theory calculations are carried out by the *Vienna ab initio Simulation Package* for $5 \times 5 \times 5$ supercells for the relaxed unit cells of diamond with $2 \times 2 \times 2$ Monkhorst-Pack k-point grids. The harmonic IFCs and phonon dispersion curve are acquired using the PHONOPY package [38]; anharmonic IFCs are calculated using code from the SHENGBTE package [39] known as THIRDORDER.PY for $4 \times 4 \times 4$ supercells with $2 \times 2 \times 2$ Monkhorst-Pack k-point grids. For this calculation, up to the fifth-nearest neighbors are considered. Diamond has a high Debye temperature of approximately 2200 K, which leads to a more normal (N) scattering of diamond near and below room temperature. Thus, a full iterative solution is computed to accurately describe the κ of strained diamond using the SHENGBTE package [39] with harmonic and anharmonic IFCs [1].

Phonons are thermal carriers in crystals. As early as 1929, Peierls developed the Boltzmann gas heat conduction theory and provided the first description of the thermal conductivities of semiconductors and insulators in microscopic terms [40]. At the temperature T, the phonon distribution in the crystal obeys the Bose-Einstein distribution in thermodynamic equilibrium state, as follows:

$$f_\lambda^0 = \frac{1}{e^{\hbar\omega/k_B T} - 1}. \tag{1}$$

A temperature gradient drives a phonon heat current by diverting phonon distribution from the equilibrium distribution, as follows:

$$f_\lambda = f_\lambda^0 - \frac{\partial f_\lambda^0}{\partial E_\lambda}\Psi_\lambda = f_\lambda^0 + f_\lambda^0\left(1 + f_\lambda^0\right)\Psi_\lambda. \tag{2}$$

The resulting nonzero phonon heat flux $\mathbf{J}$ can be expressed as follows [30]:

$$\begin{aligned}\mathbf{J} &= \frac{1}{NV}\sum_\lambda \hbar\omega_\lambda \mathbf{v}_\lambda f_\lambda \\ &= \frac{1}{k_B T^2 NV}\sum_\lambda f_\lambda^0\left(1 + f_\lambda^0\right)(\hbar\omega_\lambda)^2 \mathbf{v}_\lambda(\mathbf{F}_\lambda \cdot \nabla T),\end{aligned} \tag{3}$$

TABLE I. Bond lengths of bond12 (B12), bond13 (B13), bond14 (B14), and bond15 (B15) under strain; bond angles between bond12 and bond15 (φ215), bond13 and bond14 (φ314), bond12 and bond13 (φ213), and bond14 and bond15 (φ415) under strain.

ε	0.0%	0.1%	1.0%	10.5%
B12 = B13 = B14 = B15 (Å)	1.53106	1.53144	1.53500	1.57962
φ215 = φ314 (deg)	109.4712	109.4101	108.8699	103.6376
φ213 = φ415 (deg)	109.4712	109.5018	109.7727	112.4644

where λ includes the phonon branch index p and wave vector q; ω_λ and $\mathbf{v}_\lambda$ are the angular frequency and group velocity of phonon mode λ, respectively; $\mathbf{F}_\lambda$ is the mean free displacement of phonons; N is the number of q points in the first Brillouin zone; V is the volume of the unit cell; and T is the temperature.

According to Fourier's law $\mathbf{J}^\alpha = -\sum_\beta \kappa^{\alpha\beta}(\nabla T)^\beta$, the coefficient of thermal conductivity can be obtained as follows:

$$\kappa^{\alpha\beta} = \frac{1}{k_B T^2 N V}\sum_\lambda f^0_\lambda\left(1+f^0_\lambda\right)(\hbar\omega_\lambda)^2 v^\alpha_\lambda F^\beta_\lambda, \tag{4}$$

where $\kappa^{\alpha\beta}$ represents κ corresponding to the heat flow generated in the α direction by the temperature gradient in the β direction.

The linearized BTE $\mathbf{F}_\lambda$ can then be written as follows [39]:

$$\mathbf{F}_\lambda = \tau^0_\lambda(\mathbf{v}_\lambda + \mathbf{\Delta}_\lambda), \tag{5}$$

where $\mathbf{\Delta}_\lambda$ represents the effective change in velocity after scattering and τ^0_λ is the lifetime of mode λ, the inverse of which is the scattering rate calculated by Matthiessen's rule [41]. The phonon–phonon (anharmonic) and phonon–isotope scatterings with the natural isotopic distribution of diamond are considered. Total scattering rates $1/\tau^0_\lambda$ are determined as follows:

$$\frac{1}{\tau^0_\lambda} = \frac{1}{\tau^{\text{anh}}_\lambda} + \frac{1}{\tau^{\text{iso}}_\lambda}. \tag{6}$$

The phonon–phonon scattering rates require the identification of a set of three-phonon scattering processes that satisfy phonon energy and momentum conservation conditions, as follows [42]:

$$\omega_\lambda \pm \omega_{\lambda'} = \omega_{\lambda''} \text{ and } \mathbf{q} \pm \mathbf{q}' = \mathbf{q}'' + \mathbf{K}, \tag{7}$$

where λ, λ', and λ'' represent the three phonons involved; K is the reciprocal lattice vector. K = 0 characterizes momentum-conserving normal processes and K ≠ 0 corresponds to resistive umklapp processes [43]. However, the intrinsic three-phonon scattering rates are treated similarly ("+" represents absorption processions and "–" represents emission processions), as follows:

$$\Gamma^+_{\lambda\lambda'\lambda''} = \frac{\hbar\pi}{4}\frac{f'_0 - f''_0}{\omega_\lambda\omega_{\lambda'}\omega_{\lambda''}}\left|V^+_{\lambda\lambda'\lambda''}\right|^2\delta(\omega_\lambda - \omega_{\lambda'} - \omega_{\lambda''}), \tag{8}$$

$$\Gamma^-_{\lambda\lambda'\lambda''} = \frac{\hbar\pi}{4}\frac{f'_0 + f''_0 + 1}{\omega_\lambda\omega_{\lambda'}\omega_{\lambda''}}\left|V^-_{\lambda\lambda'\lambda''}\right|^2\delta(\omega_\lambda - \omega_{\lambda'} - \omega_{\lambda''}). \tag{9}$$

The Dirac distribution $\delta(\omega_\lambda \pm \omega_{\lambda'} - \omega_{\lambda''})$ enforces the conservation of energy in the absorption and emission processes. The scattering matrix elements $V^\pm_{\lambda\lambda'\lambda''}$ can be calculated by third-order IFCs, as follows [1,44]:

$$V^\pm_{\lambda\lambda'\lambda''} = \sum_{i\in u.c.}\sum_{j,k}\sum_{\alpha\beta\gamma}\Phi^{\alpha\beta\gamma}_{ijk}\frac{e^\alpha_\lambda(i)e^\beta_{p',\pm\mathbf{q}'}(j)e^\gamma_{p'',-\mathbf{q}''}(k)}{\sqrt{M_iM_jM_k}}, \tag{10}$$

where $\Phi^{\alpha\beta\gamma}_{ijk}$ is the anharmonic IFCs matrix. It refers to movement of the two atoms in multiple directions in the supercell, followed by calculation of the Hellmann-Feynman force after displacement.

Finally, we obtain the anharmonic scattering rates $1/\tau^{\text{anh}}_\lambda$ according to the following equation:

$$\frac{1}{\tau^{\text{anh}}_\lambda} = \frac{1}{N}\left(\sum^{+}_{\lambda'\lambda''}\Gamma^+_{\lambda\lambda'\lambda''} + \sum^{-}_{\lambda'\lambda''}\frac{1}{2}\Gamma^-_{\lambda\lambda'\lambda''}\right). \tag{11}$$

In addition to intrinsic three-phonon scattering, elastic scattering of phonons introduced by isotope impurities is present, as follows [45,46]:

$$\begin{aligned}\frac{1}{\tau^{\text{iso}}_\lambda} &= \frac{1}{N}\sum_{\lambda'}\Gamma_{\lambda\lambda'}\\ &= \frac{1}{N}\sum_{\lambda'}\frac{\pi\omega^2}{2}\sum_{i\in\text{u.c.}} g(i)\left|\mathbf{e}^*_\lambda(i)\cdot\mathbf{e}_{\lambda'}(i)\right|^2\delta(\omega_\lambda - \omega_{\lambda'}),\end{aligned} \tag{12}$$

where $g(i) = \sum_S f_S(i)[1 - M_S(i)/\overline{M}(i)]^2$ is the Pearson deviation coefficient of the masses $M_S(i)$ of isotopes s of atom i.

III. RESULTS AND DISCUSSION

A. Phonon dispersion

The accuracy of the solution is closely associated with the division of the Brillouin zone grids. We first confirm the grid independence of thermal conductivity (Fig. 2). Through comprehensive consideration of accuracy and calculation efficiency, a 31 × 31 × 31 q-point grid is used in the calculation of thermal conductivity. Convergence with the force range cutoff, *scalebroad* value [39], and the supercell size is also checked.

Figure 3 presents the phonon dispersions and phonon densities of state for unstrained and strained diamond, calculated using the harmonic IFCs. It is clear that first-principles calculations can describe phonon frequency variation completely and accurately, without the need for empirical parameters. The phonon dispersion in diamond is characterized by longitudinal optical branch overbending and the large splitting between the longitudinal optical and transverse optical phonons formed between the Γ and X points, as well as the parabolicity of the TA branches at the high-symmetry point X in comparison to kin element materials Si and Ge [47]. The high group

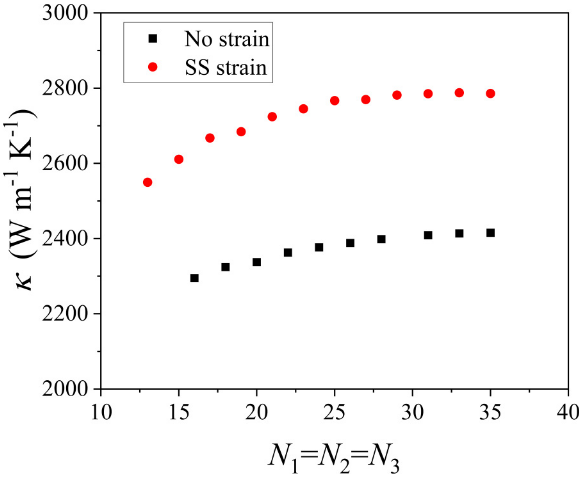

FIG. 2. Grid independence verification.

velocities and weak anharmonic scattering of phonons in diamond are closely associated with its special phonon dispersion.

The strain-dependent phonon dispersion relationships indicate that the LA branch monotonically decreases with increasing strain. Concerning the TA branches, TA1 decreases and TA2 increases under small-scale (SS; $\varepsilon = 0.1\%$) and medium-scale (MS; $\varepsilon = 1.0\%$) strains, but these changes are minimal. The separation of TA1 and TA2 branches is related to the transformation of diamond carbon atoms from the highly symmetrical regular tetrahedral structure to the ordinary tetrahedral structure. Under large-scale (LS) strains ($\varepsilon = 10.5\%$), both TA branches decrease, and TA1 is significantly lower than TA2. This leads to low group velocities, which is one of the main factors that reduces κ. Concerning the variation of optical branches, the rule remains consistent under isotropic tensile action and under uniaxial tensile action: the optical branches decrease with increasing stress. The LS strain significantly reduces the frequency of optical phonons, which usually leads to strong scattering between acoustic and optical phonons due to reduction of the band gap. This is because stress increases the distance between carbon atoms in the unit cell, thus weakening interactions among the atoms. Additionally, under LS strain, the major peak frequency of phonon densities of state decreases from 36.61 to 27.30 THz because of longitudinal optical and transverse optical branch reduction; the peak value is also smaller. Such a red shift is the result of the softened phonon vibrations. This behavior generally causes a decrease in both group velocities [48,49], thereby reducing thermal conductivity [25]. However, SS strain does not have a significant effect on optical phonon branches because of the small change in atomic interactions, with minimal red shifting of the major peak.

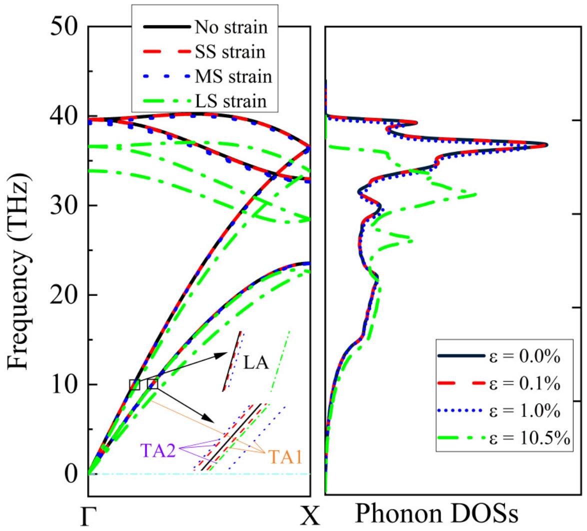

FIG. 3. Calculated phonon dispersion relationships in diamond under different tensile stresses and phonon densities of state (DOSs). (SS strain represents small-scale strain, $\varepsilon = 0.1\%$; MS strain represents medium-scale strain, $\varepsilon = 1.0\%$; LS strain represents large-scale strain, $\varepsilon = 10.5\%$).

B. Thermal conductivity

The calculated κ values of strained and unstrained diamond are plotted in Fig. 4. Figure 4(a) presents the temperature dependence of κ under uniaxial tensile stress at different scales. The calculated value of κ is in good agreement with the experimental data from Inyushkin *et al.* [5] for their bar-shaped sample with dimensions of $7.25 \times 1.54 \times 0.32\ \mathrm{mm}^3$. The application of uniaxial stress does not change the temperature dependence of diamond thermal conductivity. Phonon–phonon scattering provides most of the thermal resistance at high temperatures. In this state, increasing the temperature increases the heat occupation of phonons at all frequencies [8], leading to larger increases in the intrinsic three-phonon scattering rate and smaller values of κ. Additionally, κ behaves anisotropically. The κ along the uniaxial stretching direction ($\langle 100\rangle$) is higher than the κ perpendicular to it ($\langle 010\rangle$ and $\langle 001\rangle$). This anisotropy is not obvious for SS strain systems. Because of the large lattice deformation, the anisotropy becomes distinct at $\varepsilon = 10.5\%$ and tends to be strengthened with temperature. However, this is a common phenomenon because the atoms are arranged in different numbers and manners in different directions [50,51]. This paper does not focus on this aspect. The research focus of this paper is the abnormal response of κ under uniaxial strain; κ increases with SS strain and decreases with LS strain. The inset in Fig. 4(a) shows that the phenomenon is not observed under isotropic stretching. Such behavior, typically observed in 2D materials under stretching [20,21,22,23], results from the synergistic effects of heat capacity, group velocity, and phonon lifetime. Although these effects all occur under similar strain, this thermal response is anomalous for bulk diamond with an SS strain that has minimal effect on phonon dispersion; κ increases by up to $\sim 15\%$ at room temperature. At the low temperature of 100 K, the response is more obvious and κ is up to $\sim 36\%$ higher. This cross-scale comparison and analysis of strain–thermal conductivity dependence have been ignored by most studies. Preliminary analysis of the phonon dispersion relationship in Fig. 3 revealed that the internal mechanism of

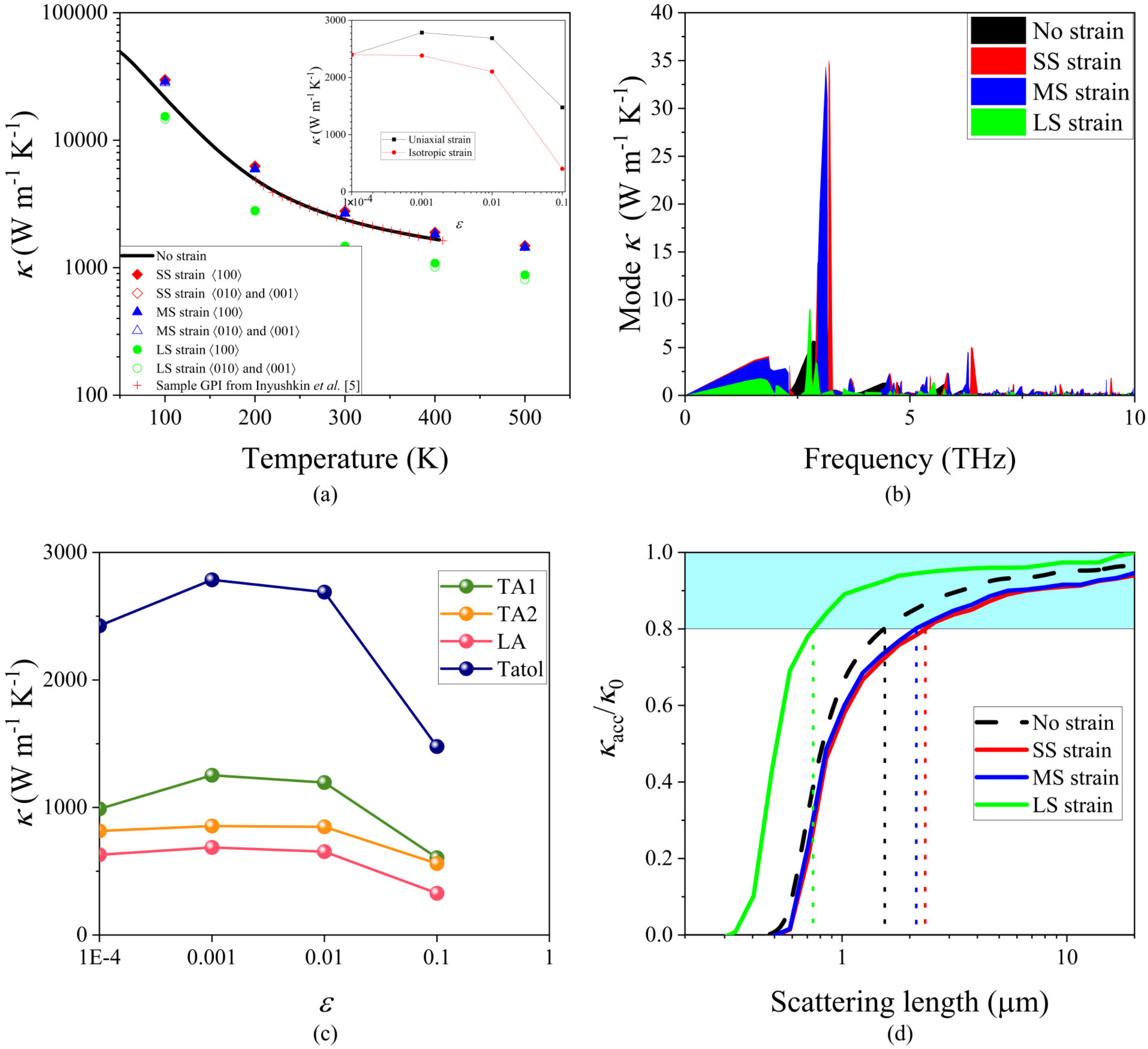

FIG. 4. (a) Temperature dependence of the thermal conductivity (κ) of diamond. The inset shows the strain dependence of κ (at room temperature, 300 K) under uniaxial and isotropic strains. (b) Mean mode κ under different tensile stresses, (c) contribution to κ from each acoustic band, and (d) normalized cumulative thermal conductivity $\kappa_{\mathrm{acc}}/\kappa_0$ of isotopically pure diamond.

the variation of thermal conductivity differs under strain at different scales.

The mode κ graph shown in Fig. 4(b) indicates that low-frequency phonons mainly contribute to κ. High-frequency phonons generally belong to the optical vibration mode with smaller group velocities and stronger phonon scattering [17]. Therefore, the optical phonon mode also has a very short mean free path (MFP). The peak value point of mode κ is (3.20, 41.95) under SS strain. The frequency varies minimally compared with the frequency under the unstrained condition, but κ considerably increases. The peak value point of mode κ is (3.16, 38.00) under MS strain, with a lower κ and frequency compared with the values obtained at 0.1% strain. The dominant phonon frequency of κ is smaller under LS strain and occurs at (2.78, 10.8). The variation rule of the mode κ of the peak point is identical to the variation rule of κ, and we presume that the variation of κ is related to the dominant heat-carrying phonons.

Figure 4(c) presents the contribution from each band to κ. The increase in κ under SS and MS strains is mainly caused by the TA1 branch. The phonon group velocities of the TA1 branch are generally low; thus, the increase in the contribution of TA1 to κ is presumably related to intrinsic anharmonic coupling between phonons. Approximately 80% of the three-phonon scattering process involves optical phonons [8]. The results suggest two reasons for this behavior. First, the reduction of TA1 under SS and MS strains will lead to a large energy band gap between TA1 and the optical branch, which will reduce the phonon scattering channels. Second, changes in bond length and energy among atoms influence the anharmonic interactions among atoms. However, the κ of the three branches significantly decreases under LS strain. The decreased κ may be caused by the large reduction of the LA branch, which leads to lower group velocities, as well as the partial increase in acoustic-optic mode scattering channels caused by the reduction of the optical branches.

TABLE II. Strain dependence of mode heat capacity.

ε	0.0%	0.1%	1.0%	10.5%
Heat capacity (10^5 J K^{-1} m^{-3})	18.442	18.452	18.554	20.318

To clarify the effects of uniaxial stress on phonon–phonon interactions, the normalized cumulative thermal conductivity $\kappa_{\mathrm{acc}}/\kappa_0$ of isotopically pure diamond is shown in Fig. 4(d), considering only intrinsic phonon–phonon scattering; κ_{acc} refers to the cumulative thermal conductivity and κ_0 is the total thermal conductivity for the corresponding case. In the absence of strain, only a small portion of the heat-carrying phonon spectrum is thermally populated [8]; a large portion of κ is contributed by phonons with short MFP (< 2 μm). The curve of the LS strain case is similar to the curve of the unstrained case, but the shift to a smaller scattering length shows that increasing the LS uniaxial strain reduces the scattering length of all mode phonons and thus reduces κ. This behavior is related to the decreases in acoustic phonon group velocities and phonon lifetime, which lead to smaller $|\tau_\lambda^0|v_\lambda$. The red and blue solid lines correspond to the $\kappa_{\mathrm{acc}}/\kappa_0$ relationship for SS and MS strains, respectively. The results show that these strains mainly affect phonons with larger intrinsic scattering lengths (> 0.8 μm). Acoustic phonons at low frequencies are coupled to optical phonons mainly through anharmonic interactions. Thus, SS and MS strains cause TA1 to decrease and weaken anharmonic interactions, thereby reducing the scattering rate of acoustic and optical phonons.

C. Mean free path, group velocity, and phonon scattering

According to the theory of ordinary gas heat transfer and the ideal gas thermal conductivity formula, we can simply express the lattice thermal conductivity as $\kappa_l = C_V\overline{v}l/3$, where C_V is the specific heat at constant volume, $\overline{v}$ is the mean group velocity of phonons, and l is the MFP of phonons. The κ of crystalline materials is closely associated with these three parameters. We analyze variations in specific heat, phonon group velocities, MFP, and lifetime in this section. Table II presents the specific heat capacities under different stress states. The SS and MS strains do not substantially influence the specific heat capacity, whereas the LS strain slightly increases this capacity. Thus, the heat capacity is not the source of this anomaly. Additionally, we analyze the squared group velocity, MFP, and lifetime at the phonon mode level in Fig. 5. Because low-frequency phonons dominate the diamond κ, we focus on the analysis of phonons with modes < 10 THz. This selection eliminates modes that are not important for thermal conductivity.

Figure 5(a) presents the squared group velocities v_λ^2 of phonons. The results show that the uniaxial tensile stress mainly affects the LA and TA1 branches. The v_λ^2 of the TA2 branch slightly increases under SS and MS strains, with almost identical amplitude, whereas it slightly decreases under LS strain. The v_λ^2 of the LA branch decreases monotonically with uniaxial tensile strain, and the reduction is proportional to the strain scale. v_λ^2 of the TA1 branch decreases slightly under SS and MS strains, while the MS strain decreases more. The significant decreases in v_λ^2 of LA and TA1 are important factors that contribute to the decrease in κ under LS strain. The v_λ^2 of LA and TA1 branches are slightly smaller under

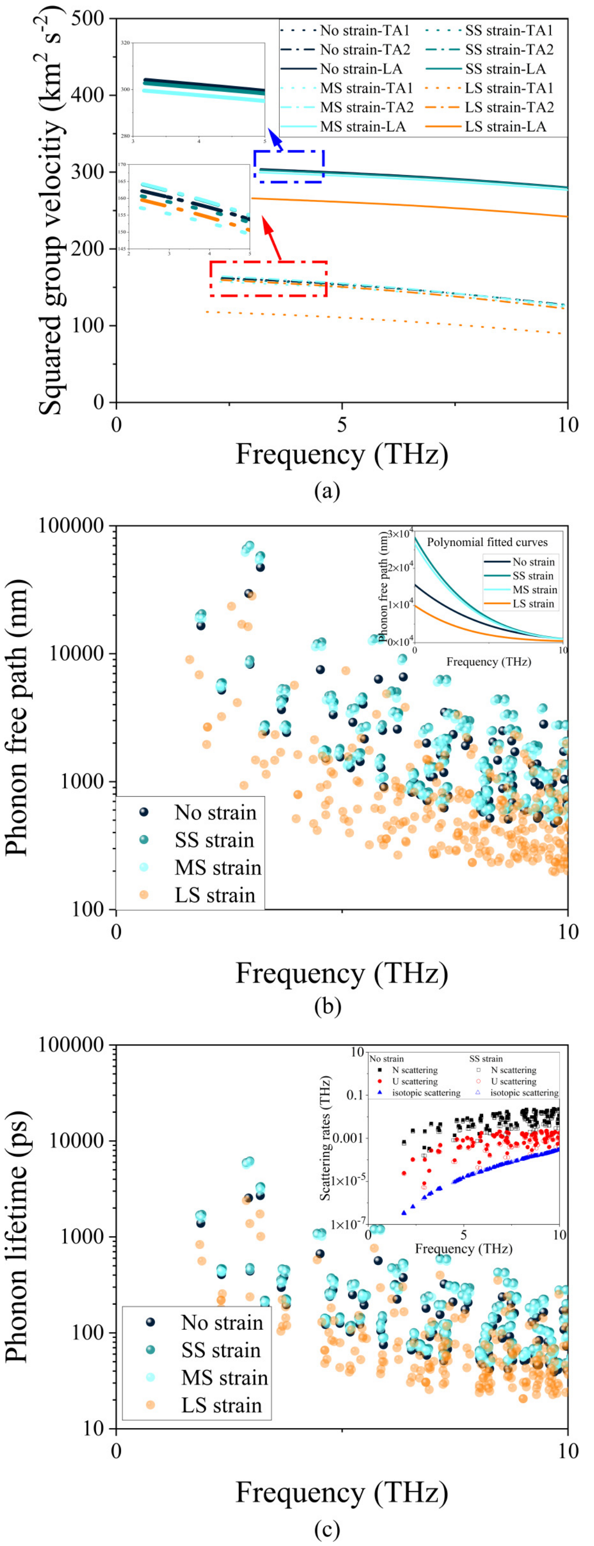

FIG. 5. Strain dependences of (a) squared group velocity, (b) phonon mean free path (The inset shows the corresponding polynomial fitted curves), and (c) phonon lifetime (The inset presents the effects of SS strain on N and U scattering).

TABLE III. Thermal conductivity obtained by different harmonic interatomic force constants (IFCs) and anharmonic IFCs.

Combination harmonic IFCs of unstrained case and different anharmonic IFCs				
ε	0	0.001	0.01	0.1
κ (W m^{-1} K^{-1})	3524.9	4032.3	4151.9	5551.6
Combination anharmonic IFCs of unstrained case and different harmonic IFCs				
ε	0	0.001	0.01	0.1
κ (W m^{-1} K^{-1})	3524.9	3507.0	3307.8	1366.8

MS strain than under SS strain, which may explain the slight difference in κ between them.

The phonon MFP and phonon lifetimes presented in Figs. 5(b) and 5(c), respectively, indicate that their variation rules are similar to the variation rules for κ. The SS and MS strains increase the MFP and lifetime of phonons, whereas LS strain clearly reduces them. Thus, the effect of strain on κ is mainly through its effect on the phonon scattering rate. The inset in Fig. 5(c) presents the effects of SS strain on N and U scattering. The SS strain reduces both U and N scattering, but it has almost no effect on isotope impurity scattering. Additionally, our calculations indicate that SS strain substantially reduces N scattering at low temperature; moreover, SS strain strongly influences phonons with long MFP, as shown in the inset in Fig. 5(b).

The effect of uniaxial strain on the scattering rate mainly refers to the effect on the three-phonon scattering rate. This effect is usually complex, and the essential phenomenon described by phonon collision comprises anharmonic interactions among atoms. Usually, stretching increases the bond lengths and decreases the bond energy between carbon atoms (Table I). Interatomic force constants characterize the local interatomic energy landscape [47]. Thus, decreased bond energy weakens anharmonic IFCs. This behavior reduces the anharmonic scattering rate of phonons, which is quadratically dependent on the force constant [17,19], as shown in Eqs. (8)–(10). Therefore, under the action of tensile strain, if other factors are constant, weakened anharmonic interactions will lead to an increase in phonon lifetimes and κ. However, in 3D bulk materials, tensile strain will not only reduce the anharmonic interactions, but also the harmonic interactions [8]. Anharmonic and harmonic IFCs generally change at the same time and affect κ concurrently; harmonic IFCs tend to enhance κ, the opposite of anharmonic IFCs. The reduction of harmonic interactions generally results in the decrease of phonon mode frequency in phonon dispersion, which will decrease phonon group velocity and increase acoustic-optic mode scattering channels, reducing phonon lifetimes. Therefore, the increase or decrease of phonon lifetimes or κ is closely related to the synergistic change of harmonic interactions and anharmonic interactions under strain. Under the action of isotropic tensile strain, the influence of harmonic interactions is usually dominant. The strain reduces phonon lifetimes. In this study, under the action of uniaxial tensile strain, as shown in Fig. 5(c), the strain at different scales has the opposite effect on phonon lifetimes, that is, SS strain and MS strain increase phonon lifetimes and LS strain decreases phonon lifetimes. Its internal mechanism will be explained in the following analysis.

Here, we confirm the actions of harmonic and anharmonic IFCs on κ by swapping force constants. Broido *et al.* exchanged IFCs between an unstrained case and the case of applied hydrostatic pressure [8]. They found that the increase in harmonic forces under hydrostatic pressure dominates κ. Table III presents κ obtained by different harmonic IFCs and anharmonic IFCs, considering only three-phonon scattering. The κ obtained by combining harmonic IFCs without stress and anharmonic IFCs under SS strain is 4032.3 W m^{-1} K^{-1}. The κ obtained by combining harmonic IFCs under SS strain and anharmonic IFCs without stress is 3507.0 W m^{-1} K^{-1}. By comparison with $\kappa_{\text{pure}} = 3524.9$ W m^{-1} K^{-1} without stress, it is evident that anharmonic IFCs contribute much more to κ, relative to harmonic IFCs under SS strain. Thus, the increase in phonon lifetime under SS strain is mainly caused by reduced anharmonic IFCs that originate from phonon softening. However, this relationship is not observed for LS strain, and the influences of harmonic IFCs and anharmonic IFCs on κ are generally numerically similar. Therefore, the main reason for the high scattering rate of LS strain may be the increased number of scattering processes allowed in diamond, which results from a change in the dispersion relationship. Enhancement of the scattering phase space will increase the phonon scattering rate [17].

Figure 6 compares the weighted phase space distribution of phonons at each frequency in the three working conditions

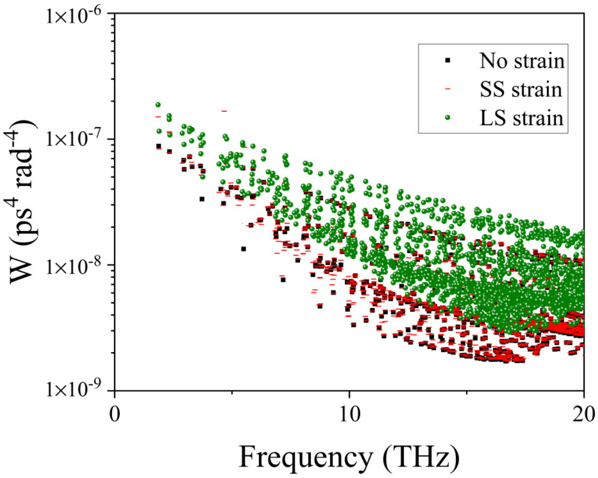

FIG. 6. Weighted phase space at room temperature as a function of frequency for strained and unstrained diamond.

of no strain, SS strain, and LS strain. The number of scattering processes available per phonon can be directly measured according to the weighted phase space. It differs from the scattering rate and depends only on phonon dispersion [52], and it can be expressed as follows [53]:

$$W_\lambda^{\pm} = \frac{1}{2N}\sum_{\lambda' p''}\left\{\begin{matrix} 2(f_{\lambda'} - f_{\lambda''}) \\ f_{\lambda'} + f_{\lambda''} + 1 \end{matrix}\right\}\frac{\delta(\omega_\lambda \pm \omega_{\lambda'} - \omega_{\lambda''})}{\omega_\lambda \omega_{\lambda'} \omega_{\lambda''}}. \qquad (13)$$

Equation (13) represents the sum of frequency-containing factors in the expression of three-phonon transition probabilities [Eqs. (8) and (9)]. The change in effective scattering channels can be confirmed by calculating W. Figure 6 shows that the weighted phase space of phonons under SS strain minimally varies, whereas the weighted phase space of phonons under LS strain becomes significantly larger. This supports the previous conjecture that the increase in phonon lifetime under SS strain is mainly caused by phonon softening, whereas the decrease under LS strains is mainly caused by the increase in phonon scattering channels related to dispersion changes.

IV. CONCLUDING REMARKS

The uniaxial strain–thermal conductivity relationships at different scales are predicted along the ⟨100⟩ crystal direction using a first-principles approach combined with the linearized phonon BTE. The thermal conductivity of diamond of natural isotopic abundance will increase by approximately 15% under SS strain of 0.1% at room temperature, which is considerable. The thermal conductivity limit is thus broken on the premise of minimally changing the mechanical properties of diamond. The underlying mechanism is that diamond anharmonic IFCs decrease under SS strain, reducing the anharmonic interactions between phonons, thereby increasing the phonon lifetime and MFP.

Under LS strain, LA and TA1 phonon group velocities are considerably reduced, and the large reduction in optical phonon branches drastically increases the phonon scattering channels, thereby increasing the phonon scattering rate. Consequently, the thermal conductivity decreases.

V. OUTLOOK

These findings will guide analyses of the dependence of thermal conductivity on strain in other diamondlike structures, such as Group IV element-based materials. The ultrahigh thermal conductivity of diamond under SS strain suggests that local strain could be used to regulate the thermal conductivities of materials by creating artificial thermal conduction channels.

ACKNOWLEDGMENTS

This work is financially supported by the National Key R&D Program of China (Grant No. 2020YFA0709700) and the Fundamental Research Funds for the Central Universities (Grant No. HIT.OCEF. 2021016).

The authors declare that they have no known competing financial interests or personal relationships that could have influenced the work reported in this study.

[1] A. Ward, D. Broido, D. Stewart, and G. Deinzer, *Ab initio* theory of the lattice thermal conductivity in diamond, Phys. Rev. B **80**, 125203 (2009).

[2] A. Bar-Cohen, J. J. Maurer, and D. H. Altman, Gen3 embedded cooling for high power RF components, in *IEEE International Conference on Microwaves, Antennas, Communications and Electronic Systems (COMCAS)* (IEEE, New York, 2017), p. 13.

[3] Y. Li, X. Liu, G. Yang, K. Liu, J. Zhao, S. Zhang, L. Yang, B. Dai, J. Zhu, and J. Han, Thinning strategy of substrates for diamond growth with reduced PCD rim: Design and experiments, Diamond Relat. Mater. **101**, 107574 (2020).

[4] H. Sumiya and K. Tamasaku, Large defect-free synthetic type IIa diamond crystals synthesized via high pressure and high temperature, Jpn. J. Appl. Phys. **51**, 090102 (2012).

[5] A. V. Inyushkin, A. N. Taldenkov, V. G. Ralchenko, A. P. Bolshakov, A. V. Koliadin, and A. N. Katrusha, Thermal conductivity of high purity synthetic single crystal diamonds, Phys. Rev. B **97**, 144305 (2018).

[6] C. Dang, J. P. Chou, B. Dai, C. T. Chou, Y. Yang, R. Fan, W. Lin, F. Meng, A. Hu, J. Zhu, J. Han, A. M. Minor, J. Li, and Y. Lu, Achieving large uniform tensile elasticity in microfabricated diamond, Science **371**, 76 (2021).

[7] C. Liu, X. Song, Q. Li, Y. Ma, and C. Chen, Superconductivity in Compression-Shear Deformed Diamond, Phys. Rev. Lett. **124**, 147001 (2020).

[8] D. A. Broido, L. Lindsay, and A. Ward, Thermal conductivity of diamond under extreme pressure: A first-principles study, Phys. Rev. B **86**, 115203 (2012).

[9] L. Lindsay, C. Hua, X. L. Ruan, and S. Lee, Survey of *ab initio* phonon thermal transport, Mater. Today Phys. **7**, 106 (2018).

[10] X. Tang and J. Dong, Lattice thermal conductivity of MgO at conditions of Earth's interior, Proc. Natl. Acad. Sci. **107**, 4539 (2010).

[11] D. A. Dalton, W. P. Hsieh, G. T. Hohensee, D. G. Cahill, and A. F. Goncharov, Effect of mass disorder on the lattice thermal conductivity of MgO periclase under pressure, Sci. Rep. **3**, 2400 (2013).

[12] K. D. Parrish, A. Jain, J. M. Larkin, W. A. Saidi, and A. McGaughey, Origins of thermal conductivity changes in strained crystals, Phys. Rev. B **90**, 235201 (2014).

[13] S. Hou, B. Sun, F. Tian, Q. Cai, Y. Xu, S. Wang, X. Chen, Z. Ren, C. Li, and R. B. Wilson, Thermal conductivity of BAs under pressure, Adv. Electron. Mater. **8**, 2200017 (2022).

[14] L. Lindsay, D. A. Broido, J. Carrete, N. Mingo, and T. L. Reinecke, Anomalous pressure dependence of thermal conductivities of large mass ratio compounds, Phys. Rev. B **91**, 121202(R) (2015).

[15] T. Ouyang and M. Hu, Competing mechanism driving diverse pressure dependence of thermal conductivity of XTe (X = Hg, Cd, and Zn), Phys. Rev. B **92**, 235204 (2015).

[16] S. Mukhopadhyay, D. Bansal, O. Delaire, D. Perrodin, E. Bourret-Courchesne, D. J. Singh, and L. Lindsay, The curious case of cuprous chloride: Giant thermal resistance and anharmonic quasiparticle spectra driven by dispersion nesting, Phys. Rev. B **96**, 100301(R) (2017).

[17] L. Zhu, T. Zhang, Z. Sun, J. Li, G. Chen, and S. A. Yang, Thermal conductivity of biaxial-strained MoS_2: Sensitive strain dependence and size-dependent reduction rate, Nanotechnology **26**, 465707 (2015).

[18] L. Zhu, W. Li, and F. Ding, Giant thermal conductivity in diamane and the influence of horizontal reflection symmetry on phonon scattering, Nanoscale **11**, 4248 (2019).

[19] L. Lindsay, W. Li, J. Carrete, N. Mingo, D. A. Broido, and T. L. Reinecke, Phonon thermal transport in strained and unstrained graphene from first principles, Phys. Rev. B **89**, 155426 (2014).

[20] Y. D. Kuang, L. Lindsay, S. Q. Shi, and G. P. Zheng, Tensile strains give rise to strong size effects for thermal conductivities of silicene, germanene and stanene, Nanoscale **8**, 3760 (2016).

[21] Y. Kuang, L. Lindsay, S. Shi, X. Wang, and B. Huang, Thermal conductivity of graphene mediated by strain and size, Int. J. Heat Mass Transfer **101**, 772 (2016).

[22] H. Xie, T. Ouyang, É. Germaneau, G. Qin, M. Hu, and H. Bao, Large tunability of lattice thermal conductivity of monolayer silicene via mechanical strain, Phys. Rev. B **93**, 075404 (2016).

[23] Y. Kuang, L. Lindsay, and B. Huang, Unusual enhancement in intrinsic thermal conductivity of multilayer graphene by tensile strains, Nano Lett. **15**, 6121 (2015).

[24] L. N. Virgin, *Vibration of Axially-Loaded Structures* (Cambridge University Press, Cambridge, 2007).

[25] Z. Ding, Q. Pei, J. Jiang, and Y. Zhang, Manipulating the thermal conductivity of monolayer MoS_2 via lattice defect and strain engineering, J. Phys. Chem. C **119**, 16358 (2015).

[26] Y. Hu, D. Li, Y. Yin, S. Li, G. Ding, H. Zhou, and G. Zhang, The important role of strain on phonon hydrodynamics in diamond-like bi-layer graphene, Nanotechnology **31**, 335711 (2020).

[27] M. Hu, X. Zhang, and D. Poulikakos, Anomalous thermal response of silicene to uniaxial stretching, Phys. Rev. B **87**, 195417 (2013).

[28] L. Felipe, C. Pereira, and D. Donadio, Divergence of the thermal conductivity in uniaxially strained graphene, Phys. Rev. B **87**, 125424 (2013).

[29] J. Antonio S. Bellido, R. Rurali, J. Íñiguez, L. Colombo, and C. Melis, Strain engineering of ZnO thermal conductivity, Phys. Rev. Mater. **3**, 065401 (2019).

[30] A. Chernatynskiy and S. R. Phillpot, Evaluation of computational techniques for solving the Boltzmann transport equation for lattice thermal conductivity calculations, Phys. Rev. B **82**, 134301 (2010).

[31] P. E. Blöchl, Projector augmented-wave method, Phys. Rev. B **50**, 17953 (1994).

[32] G. Kresse and J. Furthmüller, Efficiency of *ab initio* total energy calculations for metals and semiconductors using a plane-wave basis set, Comput. Mater. Sci. **6**, 15 (1996).

[33] J. P. Perdew and A. Zunger, Self-interaction correction to density-functional approximations for many-electron systems, Phys. Rev. B **23**, 5048 (1981).

[34] H. J. Monkhorst and J. D. Pack, Special points for Brillouin zone integrations, Phys. Rev. B **13**, 5188 (1976).

[35] K. Kunc, I. Loa, and K. Syassen, Equation of state and phonon frequency calculations of diamond at high pressures, Phys. Rev. B **68**, 094107 (2003).

[36] F. Occelli, P. Loubeyer, and R. Letoullec, Properties of diamond under hydrostatic pressures up to 140 GPa, Nat. Mater. **2**, 151 (2003).

[37] R. H. Telling, C. J. Pickard, M. C. Payne, and J. E. Field, Theoretical Strength and Cleavage of Diamond, Phys. Rev. Lett. **84**, 5160 (2000).

[38] A. Togo and I. Tanaka, First principles phonon calculations in materials science, Scr. Mater. **108**, 1 (2015).

[39] W. Li, J. Carrete, N. A. Katcho, and N. Mingo, ShengBTE: A solver of the Boltzmann transport equation for phonons, Comput. Phys. Commun. **185**, 1747 (2014).

[40] R. Peierls, Zur kinetischen Theorie der Wärmeleitung in Kristallen, Ann. Phys. **395**, 1055 (1929).

[41] G. P. Srivastava, *The Physics of Phonons* (Routledge, Oxfordshire, UK, 1990).

[42] D. A. Broido, M. Malorny, G. Birner, N. Mingo, and D. A. Stewart, Intrinsic lattice thermal conductivity of semiconductors from first principles, Appl. Phys. Lett. **91**, 231922 (2007).

[43] J. M. Ziman, *Electrons and Phonons: The Theory of Transport Phenomena in Solids* (Oxford University Press, Oxford, 1960).

[44] L. Lindsay and D. A. Broido, Three-phonon phase space and lattice thermal conductivity in semiconductors, J. Phys. Condens. Matter **20**, 165209 (2008).

[45] S. I. Tamura, Isotope scattering of dispersive phonons in Ge, Phys. Rev. B **27**, 858 (1983).

[46] D. A. Broido and T. L. Reinecke, Lattice thermal conductivity of superlattice structures, Phys. Rev. B **70**, 081310(R) (2004).

[47] G. Guo, X. Yang, J. Carrete, and W. Li, Revisiting the thermal conductivity of Si, Ge and diamond from first principles: Roles of atomic mass and interatomic potential, J. Phys. Condens. Matter **33**, 285702 (2021).

[48] X. Li, K. Maute, M. L. Dunn, and R. Yang, Strain effects on the thermal conductivity of nanostructures, Phys. Rev. B **81**, 245318 (2010).

[49] Z. Xu and M. J. Buehler, Strain controlled thermomutability of single-walled carbon nanotubes, Nanotechnology **20**, 185701 (2009).

[50] X. Liu, G. Zhang, and Y. Zhang, Surface-engineered nanoscale diamond films enable remarkable enhancement in thermal conductivity and anisotropy, Carbon **94**, 760 (2015).

[51] X. Ji, S. Matsuo, N. R. Sottos, and D. G. Cahill, Anisotropic thermal and electrical conductivities of individual polyacrylonitrile-based carbon fibers, Carbon **197**, 1 (2022).

[52] W. Li and N. Mingo, Ultralow lattice thermal conductivity of the fully filled skutterudite $YbFe_4Sb_{12}$ due to the flat avoided-crossing filler modes, Phys. Rev. B **91**, 144304 (2015).

[53] W. Li and N. Mingo, Thermal conductivity of fully filled skutterudites: Role of the filler, Phys. Rev. B **89**, 184304 (2014).